J Therm Anal Calorim (2010) 100:109–116
DOI 10.1007/s10973-009-0554-x

Thermogravimetric analysis and hot-stage Raman spectroscopy of cubic indium hydroxide

Jing Yang · Ray L. Frost · Wayde N. Martens

Received: 24 March 2009 / Accepted: 9 October 2009 / Published online: 1 November 2009

Abstract The transition of cubic indium hydroxide to cubic indium oxide has been studied by thermogravimetric analysis complimented with hot-stage Raman spectroscopy. Thermal analysis shows the transition of $In(OH)_3$ to In_2O_3 occurs at 219 °C. The structure and morphology of $In(OH)_3$ synthesised using a soft chemical route at low temperatures was confirmed by X-ray diffraction and scanning electron microscopy. A topotactical relationship exists between the micro/nano-cubes of $In(OH)_3$ and In_2O_3. The Raman spectrum of $In(OH)_3$ is characterised by an intense sharp band at 309 cm^{-1} attributed to ν_1 In–O symmetric stretching mode, bands at 1137 and 1155 cm^{-1} attributed to In-OH δ deformation modes, bands at 3083, 3215, 3123 and 3262 cm^{-1} assigned to the OH stretching vibrations. Upon thermal treatment of $In(OH)_3$, new Raman bands are observed at 125, 295, 488 and 615 cm^{-1} attributed to In_2O_3. Changes in the structure of $In(OH)_3$ with thermal treatment is readily followed by hot-stage Raman spectroscopy.

Keywords Thermogravimetry · Hot-stage Raman spectroscopy · Indium hydroxide · Indium oxide

Introduction

Indium hydroxides and oxides are a series of important semiconductor materials, which have attracted much attention in the last decade. $In(OH)_3$ is a wide-gap semiconductor with $E_g = 5.15$ eV [1], which has potential applications in photocatalytic, electronic, and solar energy fields [2–4]. While In_2O_3 is known as n-type semiconductor with a direct band gap of 3.6 eV (which is close to that of GaN [5]) and an indirect band gap of 2.6 eV [6]. In_2O_3 has been used widely as solar cells, transparent conductors and sensors [7–11].

In recent years, $In(OH)_3$ and In_2O_3 with various morphologies (e.g. nanowires [12], nanobelts [13], nanorods [14], nanotubes [15] and nanospheres [16], etc.) have been synthesised via different methods, such as chemical vapour deposition, hot-injection techniques, organic solution synthetic routes, hydrothermal methods, and solvothermal and others. It is known that cubic particles expose a specific surface, which provides an ideal model for the study of surface-related properties [17], and conversion of these cubic particles into microscale devices may provide scope for future applications. In particular, the production of indium hydroxide and indium oxide micro/nano-cubes has been realized up to now. There are several reports on synthesis of indium hydroxide micro/nano-cubes via hydrothermal routes [6, 17]. However, the characterisation on indium hydroxide and oxide micro/nano-cubes is not fully recorded yet, or appreciated, especially the thermal analysis and spectroscopic studies.

The underlying objective of this research is to synthesise an adequate indium oxide semiconductor [18–20]. The properties of these semiconductors depend very heavily on the synthesis method and preparation of the indium oxide [1, 21]. Therefore, the aim of this research is to demonstrate the use of thermal analysis and hot-stage Raman spectroscopy to assess the thermal stability of indium hydroxide, and to determine the changes in the molecular structure of the material when the indium hydroxide is

J. Yang · R. L. Frost (✉) · W. N. Martens
Inorganic Materials Research Program, School of Physical and Chemical Sciences, Queensland University of Technology, GPO Box 2434, Brisbane, QLD 4001, Australia
e-mail: r.frost@qut.edu.au

thermally treated. Such a research complements the thermal analysis and differential thermogravimetric analysis of materials [22–36]. It is reported that many factors, such as disorder, size and shape distribution, can all influence the thermoanalytical properties and vibrational properties. Moreover, the vibrational properties of semiconductors are also strongly affected by temperature. An increase in temperature introduces perturbations in the harmonic potential term, which changes the vibrational properties. Only limited thermal Raman spectroscopic studies of synthetic nanomaterials or micromaterials, for example, GaO(OH) nanorods, have been forthcoming [37]. In this study, we report the thermal analysis and hot-stage Raman spectroscopy of cubic indium hydroxide, and study the transition of cubic $In(OH)_3$ to cubic In_2O_3, relating the spectra to the structure and morphology of the synthesised materials.

Experimental

The method of preparation of the cubic indium hydroxide materials reported in our research follows self-assisted hydrothermal synthesis route, which is simply equipped and environmentally friendly, and associated with high efficiency and low cost. No surfactants or templates are used, which need to be removed later, because under the synthesised conditions, nanoparticles can undergo self-assembly and form particular structures. The electronic and optical properties of these structures are dependent on both the initial nanoparticles and the manner in which they are organized [21].

Synthesis of $In(OH)_3$ cubic materials

Analytical grade $In(NO_3)_3{\cdot}5H_2O$ and ammonia solution (28 wt%) were used as precursor to prepare the indium hydrate precipitate. $In(NO_3)_3{\cdot}5H_2O$ weighing 3 g was dissolved in 15 mL ultrapure water, and 28% ammonia was diluted into 10% solution. At room temperature, the 10% ammonia solution was added dropwise into the indium ions solution while stirring vigorously. The addition of ammonia was stopped when the pH value of the reaction mixture reached 8, and then the mixture was stirred and kept in the air at room temperature for 0.5 h. The obtained mixture was filtered, and then transferred into a Teflon vessel (125 mL) containing 2 mL ultrapure water. The Teflon vessels were sealed and heated at 180 °C for 2 days. The resulting material was washed with ultrapure water by centrifuging, and dried at 35 °C for 3 days. Finally, the obtained $In(OH)_3$ sample was calcined in a furnace at 500 °C for 4 h to form In_2O_3 product.

X-ray diffraction

X-ray diffraction (XRD) analyses were performed on a PANalytical X'Pert PRO X-ray diffractometer (radius: 240.0 mm). Incident X-ray radiation was produced from a line focussed PW3373/10 Cu X-ray tube, operating at 40 kV and 40 mA, wavelength of 1.540596 Å.

Scanning electron microscopy

The scanning electron microscopy (SEM) images were taken with a FEI Quanta 200 operating at 25 kV. The specimens were mounted on SEM mounts with carbon tape and sputter-coated with a thin layer of gold.

Raman microprobe spectroscopy

The crystals of $In(OH)_3$ were placed and oriented on the stage of an Olympus BHSM microscope, equipped with 10 and 50× objectives and part of a Renishaw 1000 Raman microscope system, which also includes a monochromator, a filter system and a Charge Coupled Device (CCD). Raman spectra were excited by a 633-nm laser at a resolution of 2 cm^{-1} in the region between 100 and 4000 cm^{-1}. Repeated acquisitions using the highest magnification were accumulated to improve the signal-to-noise ratio. Spectra were calibrated using the 520.5 cm^{-1} line of a silicon wafer. Details of the technique have been published by the authors. Spectra at elevated temperatures were obtained using a Linkam thermal stage (Scientific Instruments Ltd., Waterford Surrey, England). Spectra were taken from room temperature (25 °C) at 50 °C intervals up to a temperature of 550 °C to replicate the acquisition of data for the TGA–MS plots. Spectral Manipulation, such as baseline adjustment, smoothing and normalisation, was performed using GRAMS® software package (Galactic Industries Corporation Salem, NH, USA).

Band component analysis was undertaken using the Jandel "Peakfit" software package, which enabled the type of fitting function to be selected and allowed specific parameters to be fixed or varied accordingly. Band fitting was done using a Lorentz–Gauss cross-product function with the minimum number of component bands used for the fitting process. The Lorentz–Gauss ratio was maintained at values greater than 0.7, and fitting was undertaken until reproducible results were obtained with squared correlations of r^2 greater than 0.996.

Thermal analysis

Thermal decomposition of the indium hydroxide sample was carried out in a TA® Instruments incorporated

high-resolution thermo gravimetric analyser (series Q500) in a flowing nitrogen atmosphere (60 cm^3 min^{-1}). Approximately, 35 mg of sample underwent thermal analysis, with a heating rate of 5 °C/min, with resolution of 6 from 25 to 1000 °C. With the isothermal, isobaric heating program of the instrument, the furnace temperature was regulated precisely to provide a uniform rate of decomposition in the main decomposition stage.

Results and discussion

Thermal analysis

In order to confirm the results obtained from the hot-stage Raman spectroscopy, thermogravimetric analysis was undertaken. Figure 1 shows the typical TG–DTG curve of the synthesised indium hydroxide $In(OH)_3$. A large mass loss is observed at 219 °C. The total mass loss of 15.76% is in good agreement with the value of 16.28% calculated by assuming the following thermal decomposition: $2In(OH)_3 \rightarrow In_2O_3 + 3H_2O$. A small mass loss of 0.35% at 197 °C is observed. This mass loss step is attributed to the thermal decomposition of InO(OH), some of which is formed during the synthesis of the $In(OH)_3$. The reaction is $2InO(OH) \rightarrow In_2O_3 + H_2O$. The results of the thermal analysis are in harmony with the results inferred from hot-stage Raman spectroscopic results (see below). Both techniques show the transition occurring between 200 and 225 °C.

X-ray diffraction

X-ray diffraction was used to determine the phase structure of the as-synthesised $In(OH)_3$ and its thermally manufactured products (In_2O_3). Figure 2 shows the typical XRD patterns of the synthetic $In(OH)_3$ and In_2O_3, and all the diffraction peaks of these XRD patterns could be perfectly indexed to those of body-centred cubic $In(OH)_3$ (bbc-$In(OH)_3$) with a lattice constant $a = 7.9743$ Å (JCPDS Card No. 01-076-1463) and In_2O_3 (JCPDS Card No. 01-071-2195). Miller indices are used to label the diffraction peaks. No XRD peaks representing other crystalline phases were detected, indicating that the final product exhibited excellent crystallinity and high purity. Figure 2 also shows that the calcined product of $In(OH)_3$ is purely In_2O_3. No other materials were found. Thermal treatment of $In(OH)_3$ results in the formation of In_2O_3.

Scanning electron microscopy

Scanning electron microscopy is a well-known microscopy technique heavily used in material sciences for the study of the morphology of materials. Figure 3a and b shows comparison of the morphology of the $In(OH)_3$ with its thermally treated product In_2O_3 after treatment at 500 °C for 4 h. Figure 3a clearly shows the cubic nature of the $In(OH)_3$. The cubes are monodispersed and are between 300 and 400 nm. Figure 3b displays the morphology of the thermally treated $In(OH)_3$. It is noted that the cubic morphology is retained in the In_2O_3. It is apparent that there is a topotactical relationship between the $In(OH)_3$ and the In_2O_3 micro/nano-cubes. Some shrinkage of the micro-micro/nano-cubes is observed upon thermal treatment.

Raman spectroscopy

Many minerals both natural and synthetic lend themselves to analysis by Raman spectroscopy. The great advantage of Raman spectroscopy is that just so long as the materials are

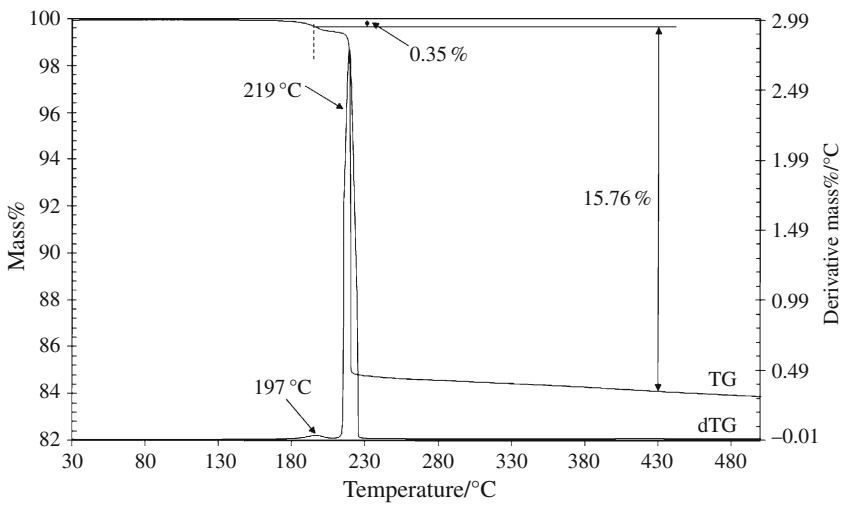

Fig. 1 Thermal analysis of $In(OH)_3$

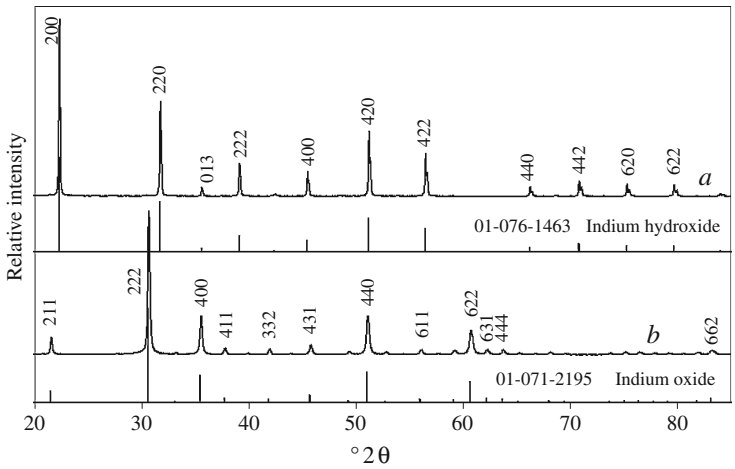

Fig. 2 XRD patterns of synthetic $In(OH)_3$ (*a*) and its thermally treated products In_2O_3 (*b*). The *peaks* are labelled with their Miller indices

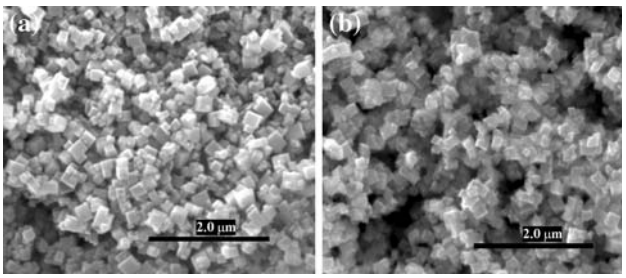

Fig. 3 SEM images of **a** $In(OH)_3$ synthesised at 180 °C, **b** In_2O_3, product of assynthetic $In(OH)_3$ calcined in a furnace at 500 °C for 4 h

1 μm in size or larger, then individual cubes can be analysed as is the case for $In(OH)_3$ as shown above. In order to study the changes in the spectra of $In(OH)_3$ as the nanomaterial is thermally treated, it is necessary to describe the spectra collected at room temperature. Figure 4 depicts the Raman spectra of cubic $In(OH)_3$ in the 100–700 cm^{-1} region. The spectrum is dominated by an intense band at 309 cm^{-1}. This band is attributed to the v_1 In–O symmetric stretching vibration. Two additional bands are found at 356 and 391 cm^{-1}. These bands are attributed to the v_3 In–O antisymmetric stretching vibrations. Low intensity bands are observed at 142, 186, 208 and 227 cm^{-1}. The three bands at 186, 208 and 227 cm^{-1} are assigned to the O–In–O bending modes. Two low intensity Raman bands are found at 660 and 670 cm^{-1}.

Figure 5 shows the Raman spectrum of cubic $In(OH)_3$ in the 950–1200 cm^{-1} region. The spectrum is composed of a broad band centred upon 1044 cm^{-1} along with two overlapping bands at 1137 and 1155 cm^{-1}. These bands are assigned to In-OH δ deformation modes. The Raman spectrum in the hydroxyl stretching region is shown in Fig. 6. A complex set of overlapping bands are observed, which may be decomposed into selected component bands at 3083, 3215, 3123 and 3262 cm^{-1}. These bands are attributed to the OH stretching vibrations.

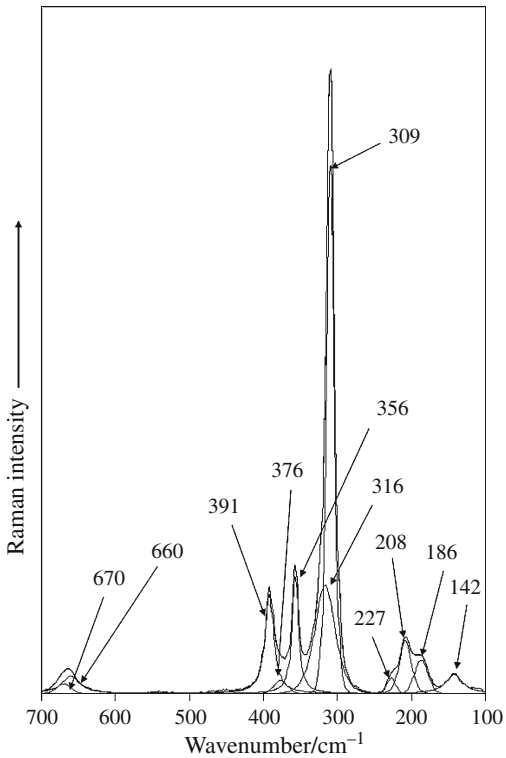

Fig. 4 Raman spectrum of $In(OH)_3$ in the 100–700 cm^{-1} region

Hot-stage Raman spectroscopy

The hot-stage Raman spectroscopy of the transition of $In(OH)_3$ to In_2O_3 in the 100–800 cm^{-1} region over the temperature range from ambient to 400 °C are displayed in Fig. 7. The base-lined and curve-resolved spectra at 150 and 400 °C, respectively, are shown in Fig. 8. The Raman spectra in Fig. 7 clearly shows the loss of intensity in the Raman bands at 137, 204, 307, 356, 390 and 659 cm^{-1} with increase in temperature. No Raman bands or bands of very low intensity are observed in the spectra collected at 300–350 °C. It is proposed that the thermally decomposed

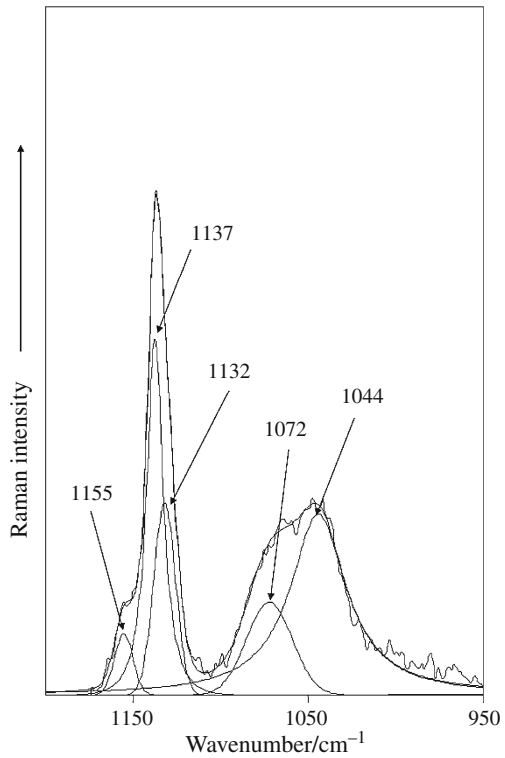

Fig. 5 Raman spectrum of $In(OH)_3$ in the 950–1200 cm^{-1} region

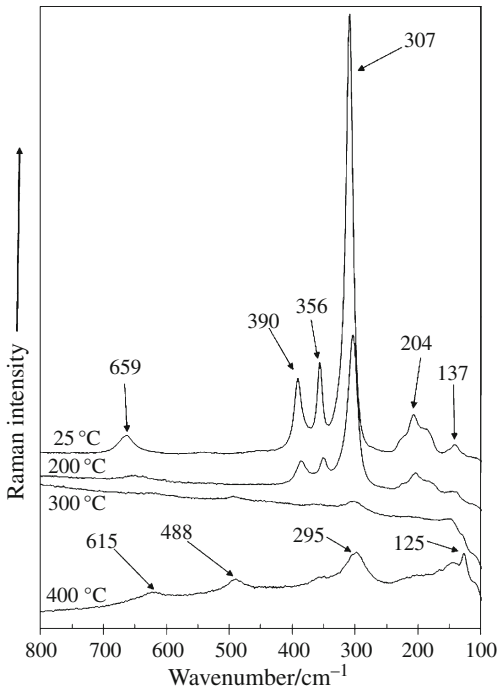

Fig. 7 Hot-stage Raman spectra of $In(OH)_3$ in the 100–800 cm^{-1} region

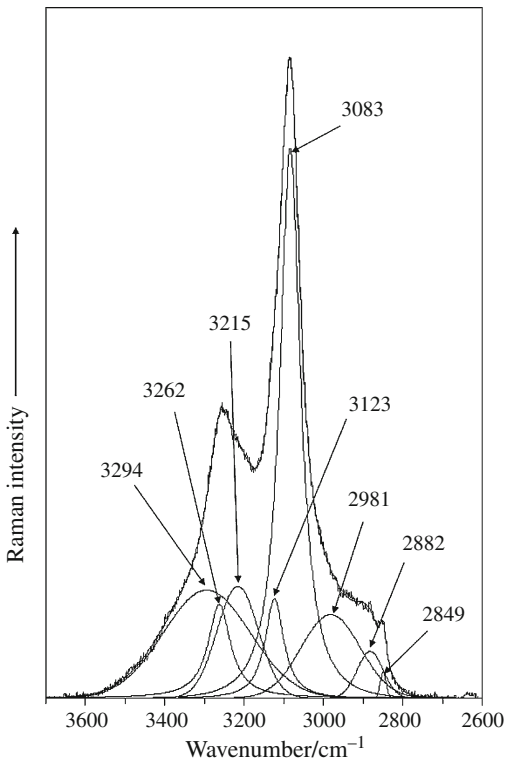

Fig. 6 Raman spectrum of $In(OH)_3$ in the 2600–3600 cm^{-1} region

indium hydroxide goes through a recrystallisation stage over this temperature range. At temperatures of 400 °C and above, new Raman peaks are observed at 125, 295, 488 and 615 cm^{-1}. These bands are attributed to the new phase formed by the thermally decomposed $In(OH)_3$, that is In_2O_3. The changes in the spectra are clearly seen in Fig. 8. According to group theory, the bands are assigned as follows: 615 cm^{-1} (E_{2g}), 488 cm^{-1} (A_{1g}), and 295 cm^{-1} (E_{1g}). According to Wang et al., Raman bands at 630, 497, 366 and 307 cm^{-1} belong to the vibrational modes of the bcc-In_2O_3. The position of the bands differs from those reported in this research. There are few articles on the Raman spectroscopy of Indium oxide. A number of phases exist. Liu et al. [38] studied the effect of pressure on the Raman spectra of In_2O_3 in the 100–700 cm^{-1} region up to a pressure of 26 GPa. These authors identified a phase transition of In_2O_3 at high pressures.

The Raman spectra in the OH stretching region at 25, 200 and 400 °C are shown in Fig. 9. Clearly, the intensity of the bands in the OH stretching region at 2844, 3079 and 3240 cm^{-1} diminish in intensity. No intensity remains in these bands at 300 °C. At 400 °C, a very weak band is observed at 3637 cm^{-1}. This weak band may be due to the OH stretching vibration of OH units from the intermediate compound InO(OH). No intensity remains in this band at 550 °C. Evidence for these changes is also observed in Fig. 10 in which the Raman spectra of the 800–1800 cm^{-1} region are displayed. Raman bands are observed at 1037

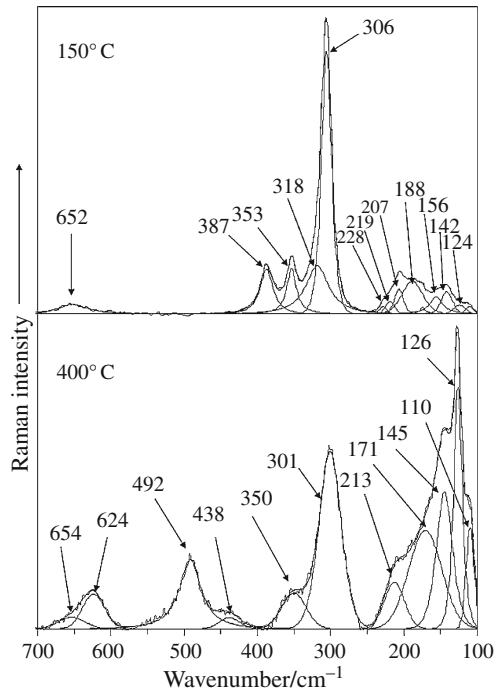

Fig. 8 The base-lined and curve-resolved Raman spectra of $In(OH)_3$ at 150 and 400 °C, respectively

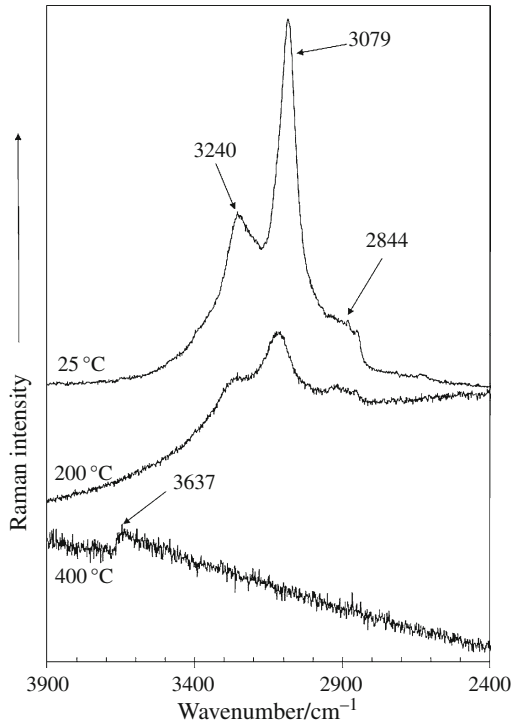

Fig. 9 Hot-stage Raman spectra of $In(OH)_3$ in the 2400–3900 cm^{-1} region

and 1135 cm^{-1} with other low intensity bands observed at 1288, 1453 and 1593 cm^{-1}. The intensity of these bands approaches zero at 200 °C. Intensity is observed only in the

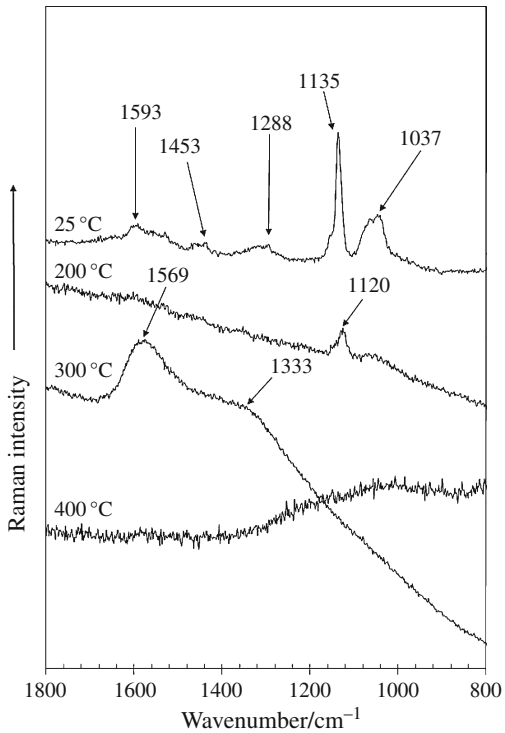

Fig. 10 Hot-stage Raman spectra of $In(OH)_3$ in the 800–1800 cm^{-1} region

band at 1120 cm^{-1}. New Raman bands appear in the 300–350 °C spectrum, respectively, at 1333 and 1569 cm^{-1}. It is thought that these bands are associated with InO(OH).

Conclusions

Micro and micro/nano-cubes of $In(OH)_3$ were synthesised by using soft chemical techniques without surfactants at low temperatures. The conversion of $In(OH)_3$ to In_2O_3 cubes was achieved by thermal treatment. The phase composition was proven by X-ray diffraction and SEM showed there was a topotactical relationship between the micro and micro/nano-cubes of $In(OH)_3$ and micro and micro/nano-cubes of In_2O_3. The transition of $In(OH)_3$ to In_2O_3 was studied by hot-stage Raman spectroscopy and thermogravimetric analysis.

The $In(OH)_3$ micro/nano-cubes are characterised by Raman spectroscopy. An Intense Raman band at 309 cm^{-1} is assigned to the v_1 symmetric stretching mode of $In(OH)_3$. The intensity of this band decreases as the temperature increases to 300 °C after which temperature which no intensity remains. A new band at 295 cm^{-1} is observed above this temperature and is attributed to the v_1 symmetric stretching mode of In_2O_3. The intensity of the two Raman bands at 3079 and 3240 cm^{-1} attributed to the OH stretching bands of $In(OH)_3$ decrease in intensity until

temperatures above 200 °C are attained after which no intensity remains. At the same time the intensity of the Raman band at 1135 cm^{-1} assigned to the δ In-OH deformation modes decrease in intensity is such that at 250 °C no intensity remains. Raman spectroscopy shows that the transition of $In(OH)_3$ to In_2O_3 occurs in the 200–225 °C temperature range. Such a transition temperature was confirmed by thermal analysis.

Acknowledgements The financial and infra-structure support from the Queensland University of Technology Inorganic Materials Research Program is gratefully acknowledged. The Australian Research Council (ARC) is thanked for funding the instrumentation. One of the authors (JY) is grateful to the Queensland University of Technology Inorganic Materials Research Program for the award of an international doctoral scholarship.

References

1. Zhuang Z, Peng Q, Liu L, Wang X, Li Y. Indium hydroxides, oxyhydroxides, and oxides nanocrystals series. Inorg Chem. 2007;49:5179–87.
2. Bayon R, Mafftiotte C, Herrero J. Chemical bath deposition of indium hydroxy sulphide thin films: process and XPS characterization. Thin Solid Films. 1999;353:100–7.
3. Bayon R, Herrero J. Reaction mechanism and kinetics for the chemical bath deposition of In(OH)(x)S-y thin films. Thin Solid Films. 2001;387:111–4.
4. Lei ZB, Ma GJ, Liu MY, You WS, Yan HJ, Wu GP, et al. Sulfur-substituted and zinc-doped In(OH)(3): a new class of catalyst for photocatalytic H-2 production from water under visible light illumination. J Catal. 2006;237:322–9.
5. Su CH, Palosz W, Zhu S, Lehoczky SL, Grzegory I, Perlin P, et al. Energy gap in GaN bulk single crystal between 293 and 1237 K. J Cryst Growth. 1237;235(2002):111–4.
6. Du JM, Yang M, Cha SN, Rhen D, Kang M, Kang DJ. Indium hydroxide and indium oxide nanospheres, nanoflowers, micro/nano-cubes, and nanorods: synthesis and optical properties. Cryst Growth Des. 2008;8:2312–7.
7. Kim H, Horwitz JS, Kushto GP, Qadri SB, Kafafi ZH, Chrisey DB. Transparent conducting Zr-doped In_2O_3 thin films for organic light-emitting diodes. Appl Phys Lett. 2001;78:1050–2.
8. Katoh R, Furube A, Yoshihara T, Hara K, Fujihashi G, Takano S, et al. Efficiencies of electron injection from excited N_3 dye into nanocrystalline semiconductor (ZrO_2, TiO_2, ZnO, Nb_2O_5, SnO_2, In_2O_3) films. J Phys Chem B. 2004;108:4818–22.
9. Zhang DH, Liu ZQ, Li C, Tang T, Liu XL, Han S, et al. Detection of NO_2 down to ppb levels using individual and multiple In_2O_3 nanowire devices. Nano Lett. 2004;4:1919–24.
10. Curreli M, Li C, Sun YH, Lei B, Gundersen MA, Thompson ME, et al. Selective functionalization of In_2O_3 nanowire mat devices for biosensing applications. J Am Chem Soc. 2005;127:6922–3.
11. Zhuang ZB, Peng Q, Liu JF, Wang X, Li YD. Indium hydroxides, oxyhydroxides, and oxides nanocrystals series. Inorg Chem. 2007;46:5179–87.
12. Li C, Zhang DH, Han S, Liu XL, Tang T, Zhou CW. Diameter-controlled growth of single-crystalline In_2O_3 nanowires and their electronic properties. Adv Mater. 2003;15:143–6.
13. Pan ZW, Dai ZR, Wang ZL. Nanobelts of semiconducting oxides. Science. 2001;291:1947–9.
14. Yang J, Lin CK, Wang ZL, Lin J. In(OH)(3) and In_2O_3 nanorod bundles and spheres: microemulsion-mediated hydrothermal synthesis and luminescence properties. Inorg Chem. 2006;45:8973–9.
15. Chen CL, Chen DR, Jiao XL, Wang CQ. Ultrathin corundum-type In_2O_3 nanotubes derived from orthorhombic InOOH: synthesis and formation mechanism. Chem Commun. 2006;4632–4.
16. Li BX, Xie Y, Jing M, Rong GX, Tang YC, Zhang GZ. In_2O_3 hollow microspheres: synthesis from designed in (OH)(3) precursors and applications in gas sensors and photocatalysis. Langmuir. 2006;22:9380–5.
17. Liu XH, Zhou LB, Yi R, Zhang N, Shi RR, Gao GH, et al. Single-crystalline indium hydroxide and indium oxide micro/nano-cubes: synthesis and characterization. J Phys Chem C. 2008;112: 18426–30.
18. Dong H-X, Yang H-Q, Yin W-Y, Yang W-Y, Wang L-F. Controlled synthesis of octahedron, nanobelts, dentate nanowires and nanocrystal chains of In_2O_3. Huaxue Xuebao. 2007;65:2611–7.
19. Du J, Yang M, Cha SN, Rhen D, Kang M, Kang DJ. Indium hydroxide and indium oxide nanospheres, nanoflowers, micro/nano-cubes, and nanorods: synthesis and optical properties. Cryst Growth Des. 2008;8:2312–7.
20. Wang C, Chen D, Jiao X, Chen C. Lotus-root-like In_2O_3 nanostructures: fabrication, characterization, and photoluminescence properties. J Phys Chem C. 2007;111:13398–403.
21. Zhu H, Yao K, Zhang H, Yang D. InOOH hollow spheres synthesized by a simple hydrothermal reaction. J Phys Chem B. 2005;109:20676–9.
22. Frost RL, Hales MC, Martens WN. Thermogravimetric analysis of selected group (II) carbonate minerals—implication for the geosequestration of greenhouse gases. J Therm Anal Calorim. 2009;95:999–1005.
23. Palmer SJ, Spratt HJ, Frost RL. Thermal decomposition of hydrotalcites with variable cationic ratios. J Therm Anal Calorim. 2009;95:123–9.
24. Carmody O, Frost R, Xi Y, Kokot S. Selected adsorbent materials for oil-spill cleanup. A thermoanalytical study. J Therm Anal Calorim. 2008;91:809–16.
25. Frost RL, Locke A, Martens WN. Thermogravimetric analysis of wheatleyite $Na_2Cu_2 + (C_2O_4)_2{\cdot}2H_2O$. J Therm Anal Calorim. 2008;93:993–7.
26. Frost RL, Locke AJ, Hales MC, Martens WN. Thermal stability of synthetic aurichalcite. Implications for making mixed metal oxides for use as catalysts. J Therm Anal Calorim. 2008;94:203–8.
27. Frost RL, Locke AJ, Martens W. Thermal analysis of beaverite in comparison with plumbojarosite. J Therm Anal Calorim. 2008; 92:887–92.
28. Frost RL, Wain D. A thermogravimetric and infrared emission spectroscopic study of alunite. J Therm Anal Calorim. 2008;91:267–74.
29. Hales MC, Frost RL. Thermal analysis of smithsonite and hydrozincite. J Therm Anal Calorim. 2008;91:855–60.
30. Palmer SJ, Frost RL, Nguyen T. Thermal decomposition of hydrotalcite with molybdate and vanadate anions in the interlayer. J Therm Anal Calorim. 2008;92:879–86.
31. Vagvoelgyi V, Daniel LM, Pinto C, Kristof J, Frost RL, Horvath E. Dynamic and controlled rate thermal analysis of attapulgite. J Therm Anal Calorim. 2008;92:589–94.
32. Vagvoelgyi V, Hales M, Frost RL, Locke A, Kristof J, Horvath E. Conventional and controlled rate thermal analysis of nesquehonite $Mg(HCO_3)(OH){\cdot}2(H_2O)$. J Therm Anal Calorim. 2008; 94:523–8.
33. Vagvolgyi V, Daniel LM, Pinto C, Kristof J, Frost RL, Horvath E. Dynamic and controlled rate thermal analysis of attapulgite. J Therm Anal Calorim. 2008;92:589–94.
34. Vagvolgyi V, Frost RL, Hales M, Locke A, Kristof J, Horvath E. Controlled rate thermal analysis of hydromagnesite. J Therm Anal Calorim. 2008;92:893–7.

35. Vagvolgyi V, Hales M, Martens W, Kristof J, Horvath E, Frost RL. Dynamic and controlled rate thermal analysis of hydrozincite and smithsonite. J Therm Anal Calorim. 2008;92:911–6.
36. Zhao Y, Frost RL, Vagvolgyi V, Waclawik ER, Kristof J, Horvath E. XRD, TEM and thermal analysis of yttrium doped boehmite nanofibres and nanosheets. J Therm Anal Calorim. 2008;94:219–26.
37. Zhao Y, Yang J, Frost RL. Raman spectroscopy of the transition of alpha-gallium oxyhydroxide to beta-gallium oxide nanorods. J Raman Spectrosc. 2008;39:1327–31.
38. Liu D, Lei WW, Zou B, Yu SD, Hao J, Wang K, Liu BB, Cui QL, Zou GT. High-pressure X-ray diffraction and Raman spectra study of indium oxide. J Appl Phys. 2008;104:083506/083 501–505.